Understanding of flow features over a typical crew module at Mach 4

S. L. N. Desikan
desikan_sln@yahoo.com
M. M. Patil and S. Subramanian
Vikram Sarabhai Space Centre
Indian Space Research Organization
Thiruvananthapuram
India

ABSTRACT

This paper presents the numerical simulations of flowfield over a typical Crew Module at Mach 4 for different angles-of-attack ranging from 0 to –25º. Detailed flow features such as contour of density gradient over the model, numerical oil flow and near wake vortex structures are captured very well in the present simulations. The location of the sonic line and its behaviour due to angles-of-attack is also captured in the simulations. The C_P distribution on the windward and leeward side shows excellent match with the experimental results. Also, the prediction of aerodynamic coefficients shows very good agreement with the experimental results. The numerical simulation predicts C_{Mcg}, C_N and C_A within 8%, 4% and 3·5% respectively with respect to experimental values.

NOMENCLATURE

C_A	axial force coefficient
C_D	coefficient of drag
C_f	coefficient skin friction
C_L	coefficient of lift
C_{Mcg}	pitching moment coefficient about centre-of-gravity
C_N	normal force coefficient
C_p	coefficient of pressure
d	base diameter, m

Paper No. 4175. Manuscript received 30 April 2014, accepted 1 November 2014.

https://doi.org/10.1017/S0001924000010794 Published online by Cambridge University Press

D	diameter, m
F_X	axial force, N
F_Y	normal force, N
k	turbulent kinetic energy
L_{ref}	reference length, m
M_{cg}	moment about centre-of-gravity, N-m
M_∞	freestream Mach number
P_∞	freestream static pressure, Pa
Re_∞	freestream Reynolds number
$+S$	co-ordinate along windward side
$-S$	co-ordinate along leeward side
S_{ref}	reference area, m^2
T_∞	freestream static temperature, K
V_∞	freestream velocity, ms^{-1}
X	co-ordinate system
Y	co-ordinate system
Z	co-ordinate system
α	angle-of-attack, deg
ε	turbulent dissipation rate
θ	boattail angle, deg
ρ_∞	freestream density, kg/m^3
τ_x	shear stress in X direction

Abbreviations

AOA	angle-of-attack
CM	crew module
FDS	flux difference splitting
ISRO	Indian Space Research Organization

1.0 INTRODUCTION

After manned space flight of Apollo, capsules have been used for re-entry through the atmosphere of Earth. Typical re-entry crew module capsule is designed to carry humans into space and bring them back safely to Earth. The crew module capsules are typically blunt body configurations with proper aerodynamic considerations. The aerodynamic characteristics of the re-entry vehicle mainly depend on flow separation, pressure behind the base and the high pressure on windward side. The high speed flow over such geometries forms a bow shock at the nose which leads to high pressure rise resulting in high aerodynamic drag. Also the flow separation and high angles-of-attack and base flow/wake structures of such capsules play a predominant role in aerodynamic characteristics. Hence such re-entry capsules have to be designed for low mass to drag ratio, large stability margin, proper design of the shoulder radius to locate the separation location and base pressure[1], transition, shear layer separation and Reynolds number effect[2], inclusion of real gas effect[3], freestream thermo-chemistry[4]. The stability is required from hypersonic to subsonic to minimise angle-of-attack excursion during severe aerodynamic heating at hypersonic condition, and to maintain a controlled attitude during parachute deployment at low speeds. This could be accomplished by sphere cone type bodies. Also, the performance of the capsule has to be ascertained

https://doi.org/10.1017/S0001924000010794 Published online by Cambridge University Press

for various conditions such as dynamic mode, aero-thermodynamic environment, free molecular, transitional and continuum regions. To predict aerodynamic and aero-thermodynamic characteristics, research has been carried out through experiments and numerical simulations at all Mach number regimes for various blunt capsule type geometries. The numerical simulations of different capsules such as ARD, CARINA, Apollo, Muses-C, OREX, Beagle-2 and spherical blunted cones show that the base pressure is independent of the fore-body configuration of the capsules[5]. The static stability of various geometries[6] are more sensitive to changes in axial shape than changes in cross section and the most stable shape is the elliptical cross section. On the other hand, at subsonic speeds, the shape of the capsule is insignificant than its edge[7]. In addition, the angle-of-attack, Mach number and Reynolds number play an imperative role in longitudinal aerodynamics[8] of the reentry capsules. It is understood that, from subsonic to supersonic Mach numbers, the flow around the re-entry capsule depends on Reynolds number[9]. Beyond certain Reynolds number, so called critical Reynolds number, the flow is independent of Reynolds number. As the Mach number increases, the critical Reynolds number decreases monotonically. Also, the base of the capsule plays a critical part and the flow structure needs to be understood. At low supersonic Mach number[10] the base flow is unsteady due to oscillations induced by the interaction of shear layer and the strong reverse base flow. On the other hand, at hypersonic condition, angle-of-attack can greatly affect the wake flow structure, base pressure, base heating. The effect of Reynolds number and enthalpies significantly affect the base region of the blunt bodies[11]. As the Reynolds number increases, the resulting heat transfer also increases. Also the heating is very sensitive to the flow total enthalpy. It is noted that the base pressure[12] on cylindrical bodies at subsonic to supersonic Mach numbers behave differently. For Mach number less than 0·8, the base pressure decreases in proportion to dynamic pressure, rapid fall in the base pressure near sonic speed and asymptotic decrease in base pressure at supersonic speeds. Base pressure depends on unsteady vortices shedding from the instability of free shear layer at subsonic flow, oscillations of front and rear local shock waves along the free shear layer at transonic flows and oscillation of free shear layer and recompression shock waves at supersonic flows. The near wake density is less than 10 and two times than the freestream for slender and blunt bodies. The number density and the pressure in the wake region is less in blunt bodies compared to slender bodies owing to shock pattern in the nose region. The translational and rotational wake temperatures are equilibrated, whereas the extent of non-equilibrium between these two temperatures with the vibrational temperature is different[13]. The impact of aerothermodynamics, heat transfer rate and radiation emission on shock stand off distance[14] and the shape of the bow shock show that the real gas effect can reduce trim angle-of-attack. It can be seen from the literature that works are carried out in continuum and transitional regimes[15,16]. Also wind tunnel and CFD data base[17-20] which includes the effect of Reynolds number is available from subsonic to hypersonic Mach numbers.

This paper presents the numerical simulation of a typical re-entry Crew Module at Mach 4 to understand the flow features at different angles-of-attack. This is one of the viable configurations of ISRO's Human Space Program for which large aerodynamic data is available from subsonic to hypersonic Mach numbers. The present simulations are carried out for the angles-of-attack ranging from 0º to –25º. Special attentions is given to understand the flow features such as separated flow structures on the model surface and near wake vortex structures at angles-of-attack. The numerical density gradients are compared with experimental Schlieren images. Comparisons of results with the experimental data[21,22] for C_p for different generators and the longitudinal aerodynamic coefficients are done.

https://doi.org/10.1017/S0001924000010794 Published online by Cambridge University Press

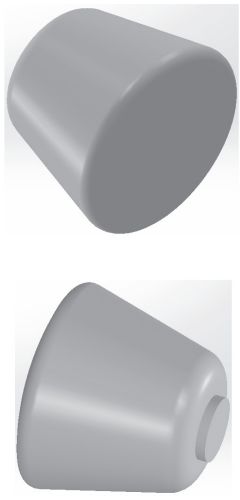


Figure 1. Sketch of crew module aeroshell configurations.

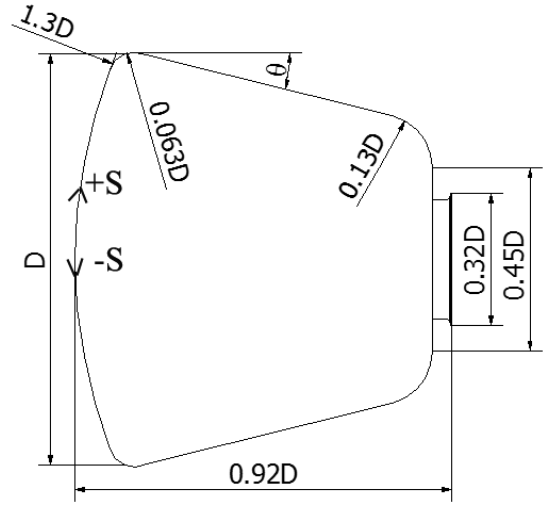


Figure 2. Schematic of crew module geometrical dimensions.

2.0 CONFIGURATION

The reentry Crew Module aeroshell configuration considered in the present study is shown in Fig. 1 and the geometrical dimensions are schematically presented in Fig. 2. The re-entry capsule is a truncated spherical configuration having a spherical nose followed by corner fillet, boat-tail and aft fillet. The maximum diameter of the geometry is D. It has a spherically blunted nose of radius 1·3D and the shoulder radius of 0·063D. The boattail angle of the body is θ and the base corner radius is 0·13D. The overall length of the body is 0·92D. The base diameter is 0·45D which is the smooth transition from the boattail base corner. Also a base cover adopter of 0·32D is provided.

2.1 Body axis system

The body axis system and schematic of the aerodynamic forces and moments are defined as shown in Fig. 3. The pitching moment coefficient (C_{Mcg}) is about the centre-of-gravity. The anti-clock rotation of the model corresponds to negative angle-of-attack. The origin (X, Y, Z) is at the centre-of-gravity of the model. The co-ordinate +S (Fig. 2) is along the top centreline (corresponds to windward side at angles-of-attack), and –S (Fig. 2) is along the bottom centreline (corresponds to leeward side at angles-of-attack).

2.2 Computational domain and grid

Figure 4 shows the grid distribution in the domain and on the model surface. The computational domain extends from –21D to +30D in x direction, –30D to +30D in y direction and 0 to 30D in Z direction. Here Z = 0 corresponds to the symmetry plane. Computations are carried out on multi block structured grid using Gambit for half model to reduce the computational time. A total of 11 blocks are used to generate the grid over the model and the total number of cells is 900,000. The surface grid distribution is based on the level of resolution required for strategic

https://doi.org/10.1017/S0001924000010794 Published online by Cambridge University Press

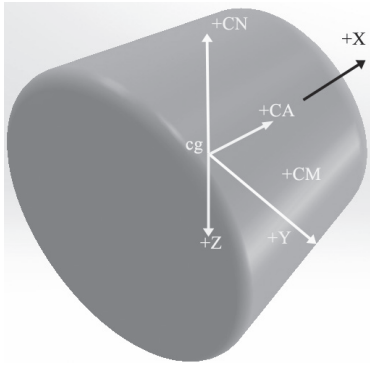


Figure 3. Sketch of body axis system.

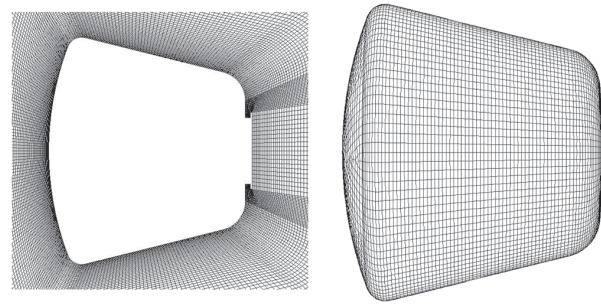


Figure 4. View of computational domain and grid.

flow physics. For example, attention is given near the stagnation point, corner fillet and aft fillet. Also, sufficient resolution and grids are provided to capture the base flow vortical structures, rapid expansion from the shoulder and the base. The first cell from the wall is of the order of 10^{-4}m with a successive ratio of 1·1 is provided to accurately predict the boundary-layer flow and uniform transition from fine to coarse grid. Also, sufficient distribution of grid is provided on the boattail region to accurately predict the local expansion followed by separation and the shear layer at high angles-of-attack. The same strategy is followed for grid independent studies with 500,000 and 17,000,000 cells respectively.

2.3 Flow solver and solution procedure

The simulations are carried out using an evaluation version of the commercial code ANSYS FLUENT. The compressible flow equations are solved using RANS with implicit, density based solver. The flow is assumed to be ideal, fully turbulent and the effect of molecular viscosity is negligible. A three coefficients Sutherland's formula is used to compute the viscosity. An implicit second order upwinding scheme is used for spatial discretisation. The entire flowfield is solved using a semi-empirical model based on model transport equations for the turbulence kinetic energy (k) and dissipation rate (ε) with default model constants and second order upwinding scheme. Along with the standard k-ε turbulence model, boundary layer is resolved by enhanced wall treatment (solve to wall). Enhanced wall treatment is a near-wall modeling method that combines a two-layer model with enhanced wall treatment. The flux splitting scheme for convective terms are evaluated by Roe flux-difference splitting (Roe-FDS) scheme. Roe-FDS splits the fluxes in a manor that is consistent with their corresponding flux method eigenvalues. The fluxes in the implicit solver are linearized with respect to all dependent variables to form the block system of equations and are solved using block Gauss-Seidel point implicit solver with an algebraic multigrid method.

2.4 Boundary conditions and flow parameters

The boundary condition applied to the entire computational domain is pressure farfield where freestream Mach number, free stream static pressure, and the freestream static temperature are prescribed. The Crew Module capsule surfaces are modelled as adiabatic with no-slip boundaries. The γ, μ_{tur}, P_{rtur}, k and ε are fixed to be 1·4, 1, 0·85, 0·8 and 0·8 in all of the computations. The flow conditions are given in Table 1.

https://doi.org/10.1017/S0001924000010794 Published online by Cambridge University Press

Table 1
Flow conditions[21,22]

Parameters	Value
Mach number (M_∞)	4
Freestream static pressure (P_∞)	5,446·8Pa
Freestream static temperature (T_∞)	70·7K
Angle-of-attack (α), deg	0, –5, –10, –15, –20, –25
Freestream Reynolds number (Re_∞)	$7{\cdot}0 \times 10^7$

Table 2
Grid independent studies at α = 0º

Grid type	No of cells	C_A	C_{Mcg}
Grid 1	500,000	1·4342	–0·02821
Grid 2	900,000	1·4329	–0·02797
Grid 3	17, 000,000	1·4322	–0·02788

2.5 Grid independent and grid convergence study

All the results presented in this paper corresponds both grid independent and grid converged solutions. Grid refinement studies are carried out to get the grid independent solution. To ascertain the solutions are independent of grid density and its distribution in X, Y and Z directions, three cases such as Grid 1 (500,000 cells), Grid 2 (900,000 cells) and Grid 3 (17,000,000 cells) are considered. The density of grids in X, Y and Z directions are varied for α = 0º case. The results of the grid refinement study are summarised in Table 2. The results show only marginal differences in aerodynamic coefficients. However, all the simulations are carried out with Grid 2 (900,000 cells).

The wall pressure along the line $Y = Z = 0$ is an appropriate representation for estimating the effect of grids because its distribution depends upon bow shock from the nose, large expansion from the shoulder, flow separation, expansion from the aft fillet and the base flow. Figure 5 shows computed coefficient of pressure along the line $Y = Z = 0$ for three girds namely Grid 1, Grid 2 and Grid 3. It can be seen that the differences between solutions on the Grid 1 and Grid 2 are quite small. Even for the Grid 3 with substantially more points, the differences remain small. Hence it is ascertained that the number of cells used for the computation of flow over the re-entry Crew Module is independent of grid and Grid 2 would be adequate enough to resolve the flow.

Also it can be seen from Fig. 6 that the computed wall y^+ for the Grid 2 (900,000 cells) shows value less than 10. The computational grid is aimed for force analysis and understanding the flowfield in mind. Hence the achieved y^+ of the order of 1-10 is acceptable for resolving the separated flows and shear layer effect which are very important for the prediction of forces. Similar observations are reported by Liever *et at*[16]. The wall y^+ distribution on the model shown in Fig. 6 for Grid 2 shows clearly the wall y^+ of the order of 5 on the boattail surface. Whereas, the aft fillet region shows the value of the order of 1-3. However, on the other hand, the shoulder region experiences marginally higher values of wall y^+ of the order of 6-10.

https://doi.org/10.1017/S0001924000010794 Published online by Cambridge University Press

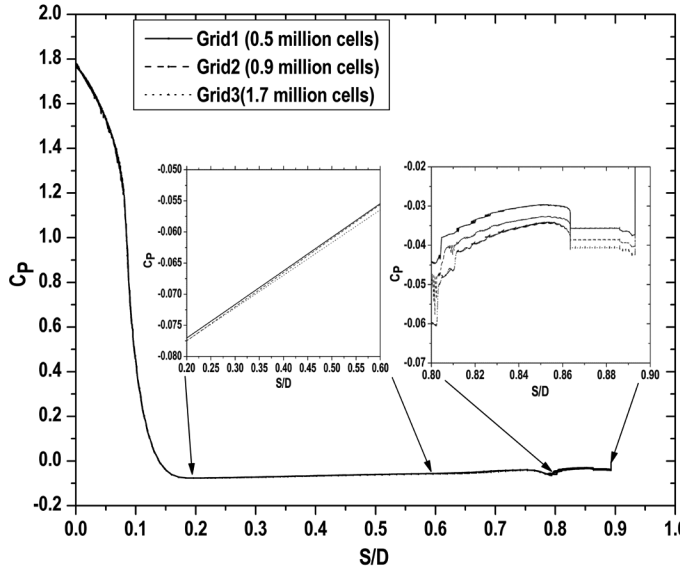


Figure 5. Effect of grid on coefficient of pressure at α = 0, $Y = Z = 0$.

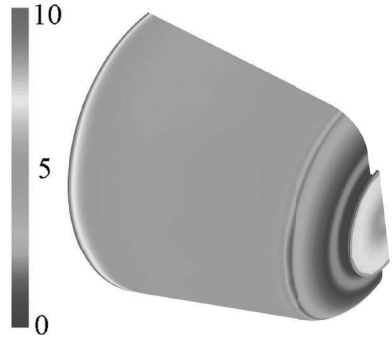
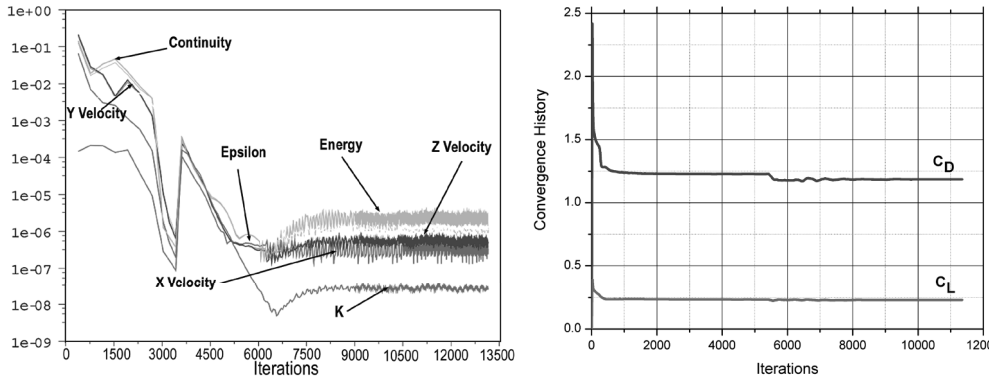


Figure 6. Contour of Wall y^+.

To assess solution convergence, residual equations and the aerodynamic coefficients (C_L and C_D) are monitored during iterations. It is assumed that the solution is converged when the residuals drop more than four orders of magnitude and the aerodynamic coefficients are flattened for enough time. Figure 7(a) shows the convergence log for Navier Stokes equation for nominal grid where the residuals drop is found to be more than four orders of magnitude. Figure 7(b) shows the convergence history of C_D, C_L for the nominal grid. It can be observed that the solutions are assumed to be converged after 8,000 iterations. Initially the solutions are first order accuracy. Once the solution reaches the steady state, the second order is turned on. This can be seen in the Fig. 7 that up to 5,500 iterations, the solutions are steady except some oscillations are seen in the initial stage. Once the second order is initiated after first order is well converged after 4,750 iterations, a drop in the coefficients are seen followed by initial oscillations. The solution becomes steady after 8,000 iterations. However the computations are carried out for enough time to see the solutions are completely constant.

https://doi.org/10.1017/S0001924000010794 Published online by Cambridge University Press



(a). Convergence of residuals. (b). Convergence of lift and drag coefficients.

Figure 7. Grid convergence history.

3.0 RESULTS AND DISCUSSION

3.1 Flowfield – density gradient

Experimental schlieren images and simulated density gradient of shock structures over the Crew Module at six angles-of-attack are shown in Figs 8-13. The flow is from left to right and, top and bottom of the Crew Module are windward and leeward side respectively. In general, the bow shock, expansion from the shoulder, expansion from the base and the shear layer are well captured. As expected, the flow is more compressed on the windward as the angle-of-attack increases. This is marked by the bow shock which is very close to the windward shoulder. On the other hand, due to flow expansion, the bow shock moves away from the body shoulder on the leeward side for increasing angles-of-attack. Also it can be seen that at angles-of-attack, the bow shock appears to be spherically shaped on the windward side and more conically shaped over the leeward side. Another important aspect of the flow feature is the shear layer separation. At 0º and –5º angles-of-attack as shown in Figs 8-9, the flow is fully attached and the shear layers on windward as well as leeward side starts at the base of the body and converges downstream of the base to form reattachment shock. However, small difference the way in which the shear layer converges at the base in the numerical prediction is observed as compared to the experimental Schlieren images. This may be due to the effect of sting at base in the experiment which is not simulated in the numerical simulations because the presence of the sting will modify the base flow. One of the objectives in the present study is to understand the flow structures in the base/wake region and the simulations require the base of the model should be free from the sting. Hence the sting is not provided in the present simulations. Nevertheless, this may not contribute appreciable impact on the aerodynamic coefficients.

Figures 10-13 show the flowfield comparison of density gradient between the prediction and the experimental Schlieren images for –10, –15, –20 and –25º angles-of-attack. The numerical simulations could reproduce the flow features which are captured through Schlieren flow visualization. The bow shock, expansion from the shoulder on both windward and leeward, and also the expansion from the base region on the leeward side is captured very well. Unlike in the case of 0 and –5º, the shear layer is captured very well in the simulations. It can be seen that the flow separation at the shoulder of the leeward side is observed from –10º onwards. In all the cases above –10º, the separation point is at the leeward shoulder of the model.

https://doi.org/10.1017/S0001924000010794 Published online by Cambridge University Press

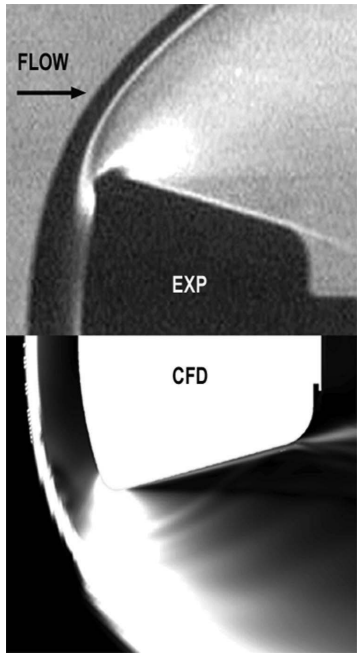


Figure 8. Density gradient at α = 0º.

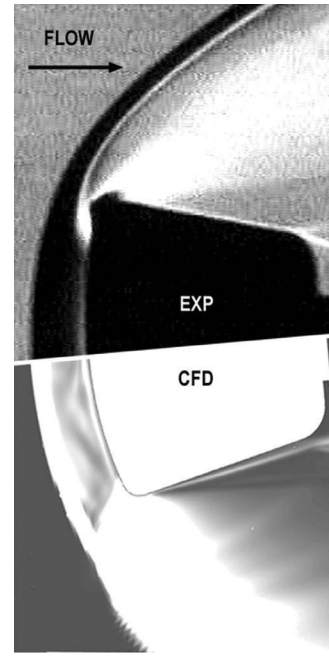


Figure 9. Density gradient at α = –5º.

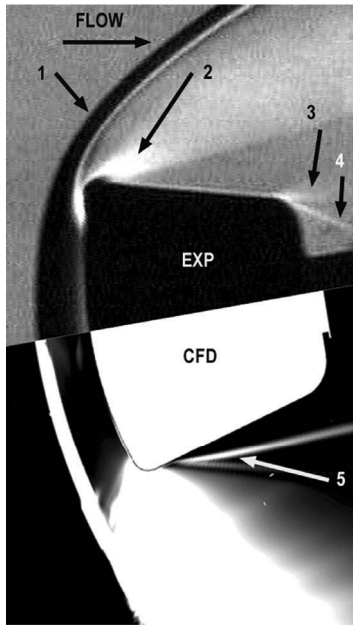


Figure 10. Density gradient at α = –10º.

1. Bow shock, 2. Expansion from shoulder, 3. Expansion from base, 4. Shear layer, 5. Shear layer separation from the leeward shoulder

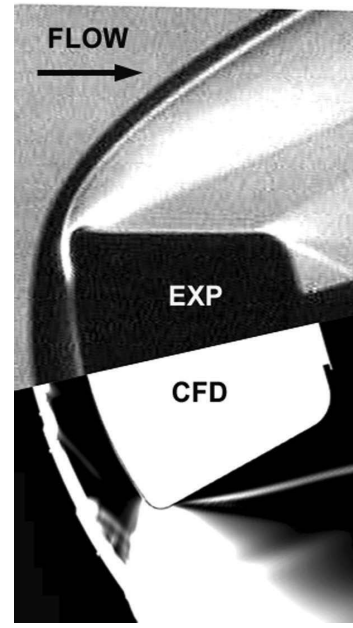


Figure 11. Density gradient at α = –15º.

https://doi.org/10.1017/S0001924000010794 Published online by Cambridge University Press

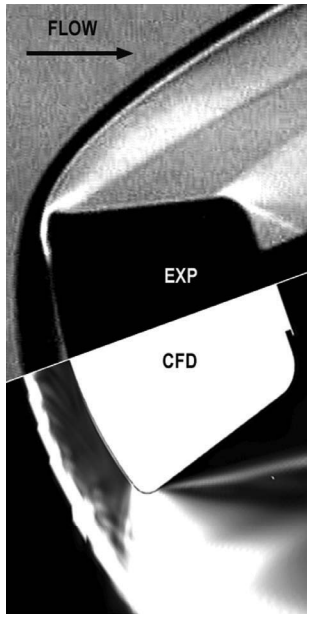


Figure 12. Density gradient at α = –20º.

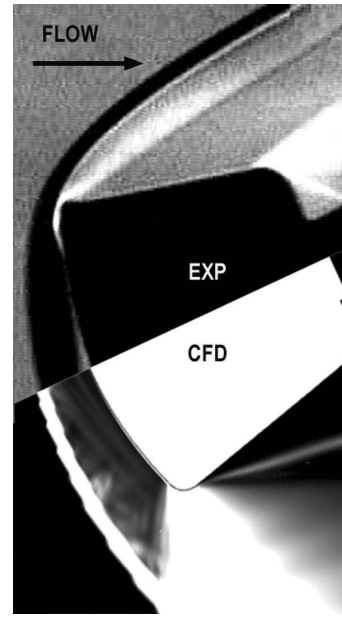


Figure 13. Density gradient at α = –25º.

3.2 Location of bow shock and sonic line

In order to understand the behaviour of sonic line and the bow shock at angles-of-attack, position of the bow shock and the sonic line which are extracted from numerical simulations for angles-of-attack ranging from 0 to –25º are presented in Fig. 14. It is observed that the bow shock moves closer to the body at the windward side due to flow compression for increasing angles-of-attack. However, more expansion takes place at leeward side due to increasing angle-of-attack makes the bow shock moves away from the body. This effect is reflected in the sonic line shape. In the windward side, the thickness of the sonic region decreases as the angles-of-attack increases and, the size increases in the leeward side at higher angles-of-attack. On the other hand, the location of the sonic line at 0º AOA in the windward side is just ahead of the model shoulder. It is observed that the location of the sonic line moves forward (towards shoulder) at higher angles-of-attack. In the leeward side, initially the sonic line position is at the shoulder of the model. As the angle-of-attack increases, the sonic line position moves backward (away from shoulder).

3.3 Numerical oil flow and flow separation

It is observed from numerical density gradient and experimental schlieren images that the flow separates from leeward side for angles-of-attack greater than –5º. To understand the separated flow on the leeward side, numerical oil flow represented by particle trace is extracted and presented in Fig. 15 for angles-of-attack ranging from 0 to –25º. Though the simulations are carried out for half symmetry, information in the symmetric plane are also synthesised in the leeward side as shown in Fig. 15, so that the entire leeward side flow pattern could be understood. The flow is from left to right. At 0º angle-of-attack, the flow is completely attached and is represented by the lines attached throughout the leeward side except a very small region near

https://doi.org/10.1017/S0001924000010794 Published online by Cambridge University Press

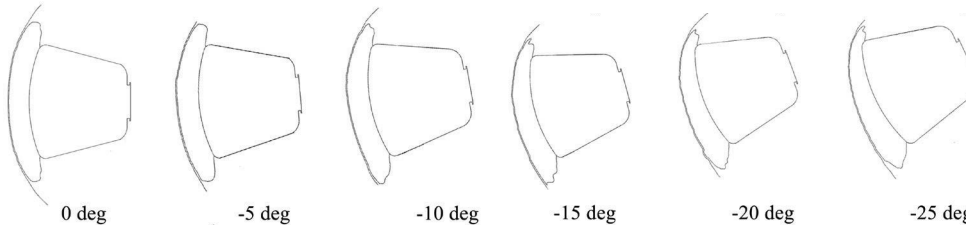


Figure 14. Position of bow shock and sonic line.

the base where the shear layer originates. Similar observations are noticed for –5º AOA where the flow is completely attached. However, the shear layer in this case is slightly moved upstream from the base. Hence the rear portion experiences a small separation. Similar observations are captured in schlieren flow visualisation and simulated density gradient (Fig. 9). At –10º AOA, the flow on the leeward side is unable to negotiate the adverse pressure gradient, separates downstream of the model shoulder. On the other hand, the high pressure on the windward side due to compression accelerates the flow from windward side to the low pressure region exits at the leeward side. The turning of the flow from windward to leeward side forms a vortex just ahead of the base of the model. The flow on the leeward side ahead of the separation also moves around the separated region upto to the base of the model and enter into the separated region. Similar observations hold good for other angles-of-attack namely –15, –20 and –25º. It should be noted that, as the angle-of-attack increases, the separation becomes larger and moves towards the upstream shoulder of the model. Also, the vortex formed in the separated region becomes large and moves upstream for increasing angle-of-attack.

To substantiate the flow separation on the leeward side due to increasing angle-of-attack, skin friction coefficient (C_f) along the line $Y = Z = 0$ for $+S$ is derived from the numerical simulations and are presented in Fig.16.

$$C_f = \frac{\tau_X}{\frac{1}{2}\rho_\infty V_\infty^2} \qquad \ldots (1)$$

At 0º AOA, the distribution of skin friction coefficient on the leeward side shows the flow is attached except at the base region. Around $S/D = 0{\cdot}71$, the coefficient changes its sign indicate that the flow is separated. This is the point the numerical oil flow result (Fig. 15) and the density gradient images (Fig. 10) also show the similar trend. As the angle-of-attack is increased from 0 to –5º, the flow is still attached to the surface and a separation is seen just ahead of the base shoulder i.e. at $S/D = 0{\cdot}68$. This trend is also captured in the numerical oil flow (Fig. 15) and the density gradient images (Fig. 9) as discussed earlier. As the angle-of-attack is increased further to –10º, the separation point moves closer to the forward shoulder of the model at $S/D = 0{\cdot}22$. Further increase in angle-of-attack ($\alpha = -15º$), the separation point moves upstream at $S/D = 0{\cdot}18$. Beyond –15º angles-of-attack, the separation point movement is not strongly pronounced which means the separation point is anchored. Similar observations are seen from numerical oil flow (Fig. 15) and the density gradient images (Figs 12 and13). Hence it can be presumed that the upstream movement of the separation point is not sensitive beyond –15º angle-of-attack.

https://doi.org/10.1017/S0001924000010794 Published online by Cambridge University Press

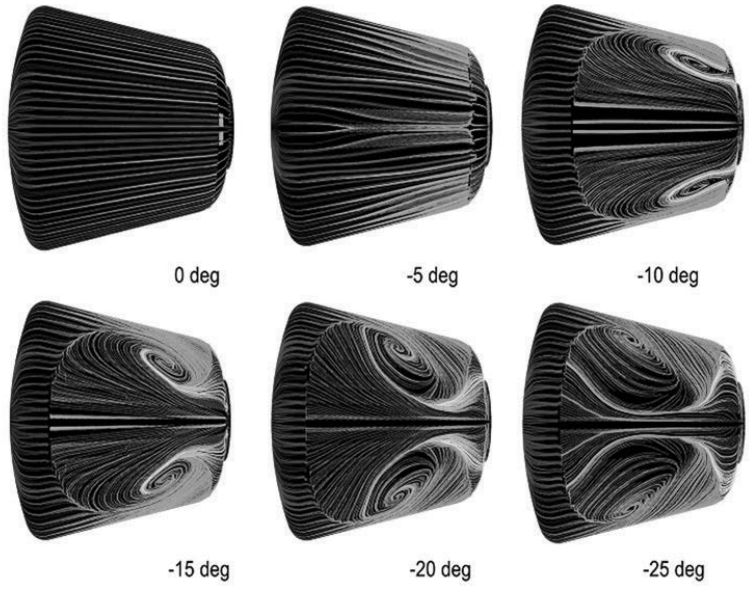


Figure 15. Numerical oil flow over the leeward side.

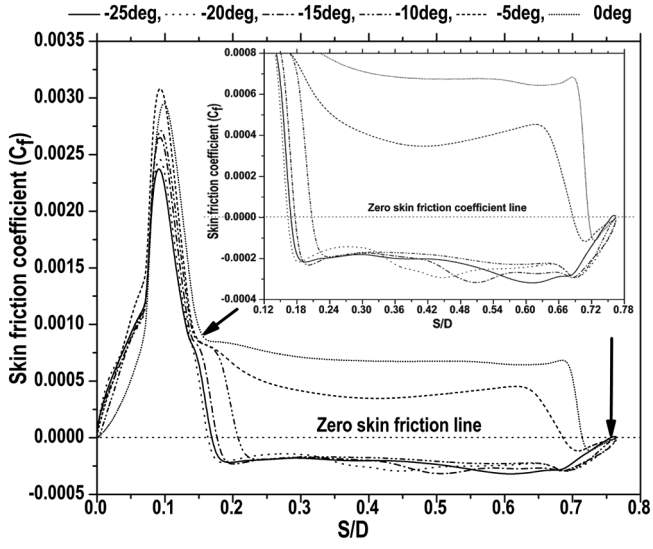


Figure 16. Skin friction coefficient along $Y = Z = 0$ line for $+S$.

3.4 Base flow features

The wake/base flow behind the blunt bodies, like Crew Module, influences the stability and base heating. Although the effect of base pressure has a little role to the total drag, the control of vehicle trajectory demands accurate prediction of base pressure[13] and base flow structures. This requires a clear understanding of wake/base flow structures. Figure 17 shows the flow over the Crew Module

https://doi.org/10.1017/S0001924000010794 Published online by Cambridge University Press

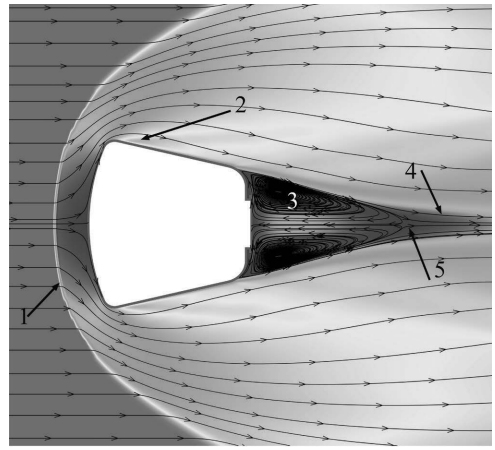


Figure 17. Mach contour with streamlines at α = 0º at symmetry plane (*Z* = 0).
1. Bow shock, 2. Expansion from shoulder, 3. Re-circulation bubble, 4. Shear layer, 5. Dividing streamline

at α = 0º depicted by Mach contour along with streamlines. The flow physics consists of a detached bow shock from the nose of the model causes a sudden increase in pressure, temperature and density, rapid expansion of the flow from the model shoulder starts from the leading edge wave and ends at a trailing edge wave, formation of the shear layer under the influence of viscous and pressure forces, recirculation bubbles at the base and formation of re-compression shock downstream of the base. Also the formation of the dividing streamline from base shoulder which separates the recirculation region from the outer flow.

3.5 Near wake flowfield

In the near wake region, recirculation is a main flow feature which is separated from the freestream by a dividing streamline as explained in Fig. 17. This dividing streamline is located in a free shear layer region[23] where the velocity of the flow is zero, shown in Fig. 18. The figure depicts the

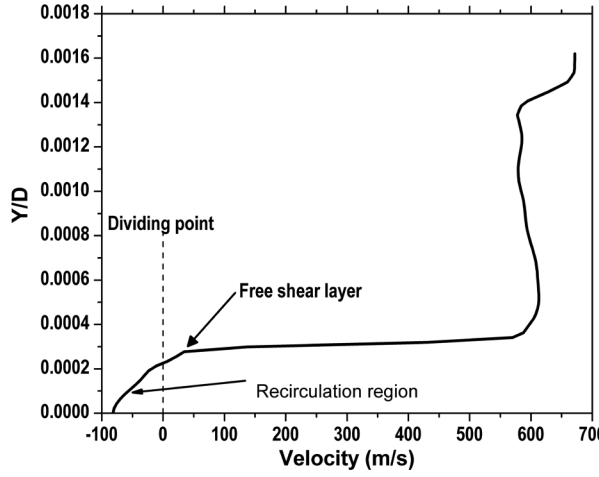


Figure 18. Typical velocity profile in the near wake region (*X*/*D* = 0·92).

https://doi.org/10.1017/S0001924000010794 Published online by Cambridge University Press

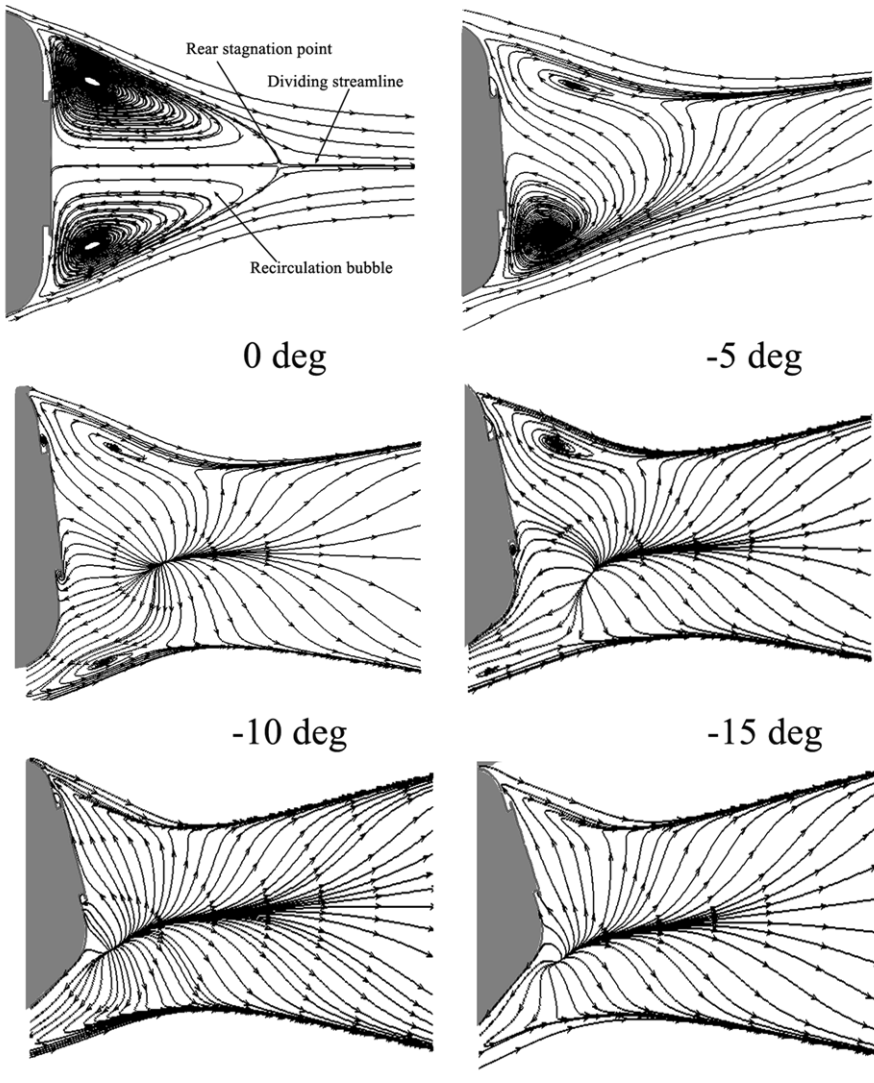


Figure 19. Near wake vortex structure.

computed X velocity at a distance 0·92D downstream of the base. The velocity is computed from Y/D = 0 to 0·0018 where the velocity reaches the freestream value. The computed free shear layer velocity profile as shown in Fig. 17 is consistent with the base flow features reported in the literature[23]. It can be seen that the values of velocities less than zero indicate the existence of vortex in the recirculation region. The vortex mechanism in the recirculation region depends on the expansion from the base shoulder. Also the flow parameters such as pressure, density and temperature in the recirculation region are totally different from other regions, it is inevitable to characterize the size of the recirculation bubbles in the near wake region.

Figure 19 shows the near wake vortex structures for angles-of-attack ranging from 0º to –25º. At $\alpha = 0^{\circ}$, a symmetric vortex pattern is observed immediately behind the wake. With respect

https://doi.org/10.1017/S0001924000010794 Published online by Cambridge University Press

to the base centreline, the two vortices are counter rotating in nature and the stagnation point of the wake is located at a distance approximately 0·9*d* from the base. Immediately adjacent to the wake stagnation point is a so called dividing streamline which separates the recirculation region from the outer supersonic flow. At angles-of-attack the vortex structure in the near wake region is getting altered. The symmetric nature of the vortex in the near wake region at $\alpha = 0^{\circ}$ no longer exists in angles-of-attack where asymmetric vortex structures are observed, which strongly depend on the expansion from the base shoulder. For example, at $\alpha = 0^{\circ}$, a strong vortex in the leeward side is seen whereas on the windward side, comparatively weak vortex is seen which is located downstream of the leeward side vortex. As the angles-of-attack increases namely $\alpha = -10$ and -15°, the vortexes are seen on both windward and leeward side of the near wake region. The strength of the vortexes on both windward and leeward sides appeared to be weak and moves upstream. However, at higher angles-of-attack such as $\alpha = -20$ and -25°, the near wake region does not show any vortex structure. Probably the vortexes could have entered into the separated region of the surface.

3.6 Comparison of coefficient of pressure (C_p)

The flow features over the crew module is explained qualitatively in the preceding paragraphs. In order to quantitatively compare the predicted results with the experimental values, coefficient of pressure along two generators namely 0 and 90º as shown in Fig. 20 are extracted and compared with the experimental values. Figure 21 shows the comparison of computed C_P in windward and leeward side for angles-of-attack ranging from 0 to –25º along 0º generator. In all the cases, the comparison is excellent. At 0º AOA, the maximum C_P is found to be 1·8 at the centre of the capsule and decreases rapidly both in windward and leeward side due to expansion from the shoulder. It can be seen that the expansion of the flow is in such a way that the value of C_P decreases below the ambient. As the angles-of-attack increases, the stagnation point (corresponds to C_P =1·8) moves towards the shoulder of the capsule. This is evident from the distribution of C_P that in the windward side at angles-of-attack greater than 0º, the value of C_P is initially lesser than 1·8 then increases to the maximum value and decreases rapidly due to expansion from the shoulder. Similarly the comparison of C_P along 90º generator is presented in Fig. 22. The results show excellent comparison with the experimental values. It can be seen that as the angles-of-attack increases, maximum value of C_P decreases. Also, rapid expansion from the shoulder is clearly visible and the value becomes lower than the freestream immediately downstream of the shoulder which is indicated by the C_P value less than zero and then the flow tries to recover thereafter.

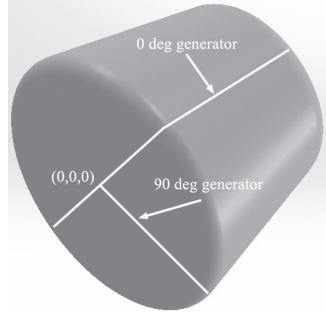


Figure 20. Co-ordinates for wall static pressure.

https://doi.org/10.1017/S0001924000010794 Published online by Cambridge University Press

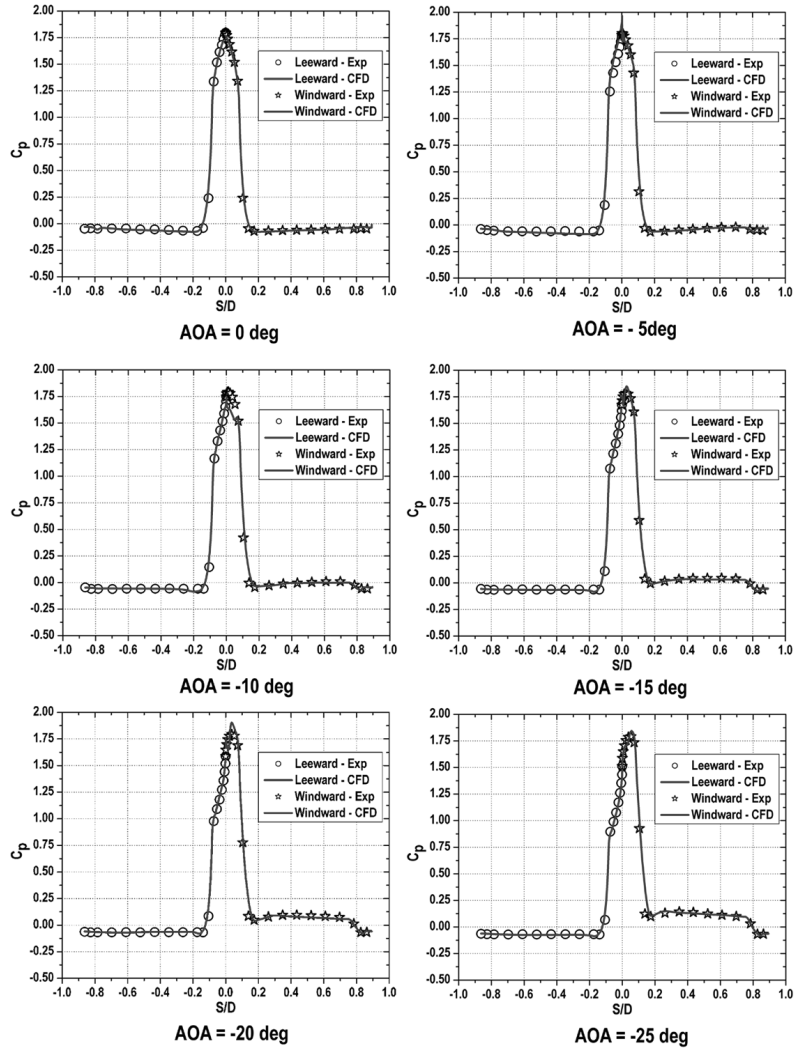


Figure 21. Comparison of C_P along 0^o generator.

3.7 Comparison of aerodynamic coefficients

The aerodynamic coefficients are analysed in terms of C_A, C_N and C_{Mcg} since they are the primary parameters to decide characteristics of the capsule and are defined by;

$$C_A = \frac{F_X}{\frac{1}{2}\rho_\infty V_\infty^2 S_{ref}} \quad \ldots (2)$$

$$C_N = \frac{F_Y}{\frac{1}{2}\rho_\infty V_\infty^2 S_{ref}} \quad \ldots (3)$$

https://doi.org/10.1017/S0001924000010794 Published online by Cambridge University Press

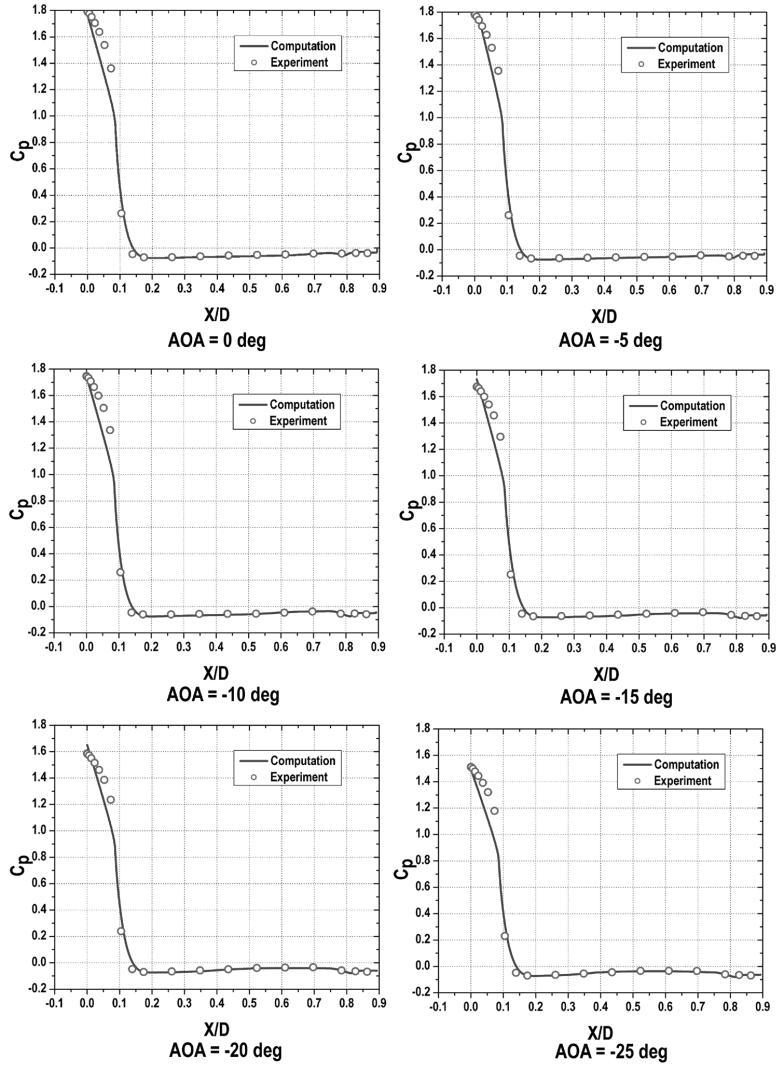


Figure 22. Comparison of C_P along 90° generator.

$$\frac{M_{cg}}{\frac{1}{2}\rho_\infty V_\infty^2 S_{ref} L_{ref}} \quad \ldots (4)$$

The reference parameters selected for the definition of aerodynamic coefficients are the longitudinal reference length (L_{ref}) which is the maximum diameter of the capsule D and the reference area S_{ref} is the maximum cross-sectional area ($\pi D2/4$) of the capsule. The pitching moment is with respect to the centre-of-gravity of the vehicle. The comparison curve of C_A, C_N and C_{Mcg} between the prediction and the experimental results for angles-of-attack ranging from 0 to –25° are shown in Figs 23-25, respectively.

As shown in Figs 23-25, the trends of all the coefficients are consistent with the experimental

https://doi.org/10.1017/S0001924000010794 Published online by Cambridge University Press

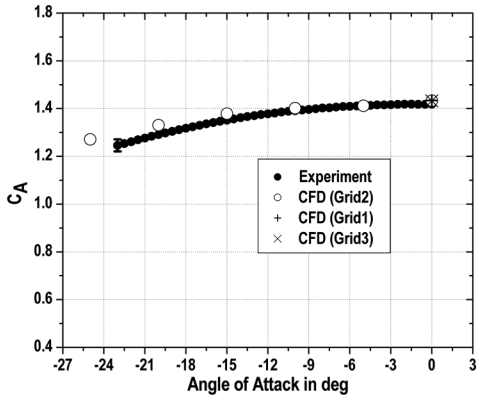


Figure 23. Comparison of C_A.

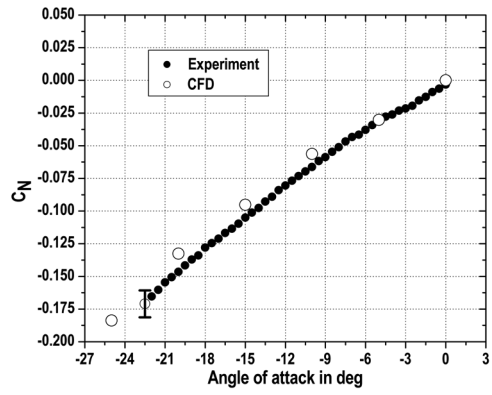


Figure 24. Comparison of C_N.

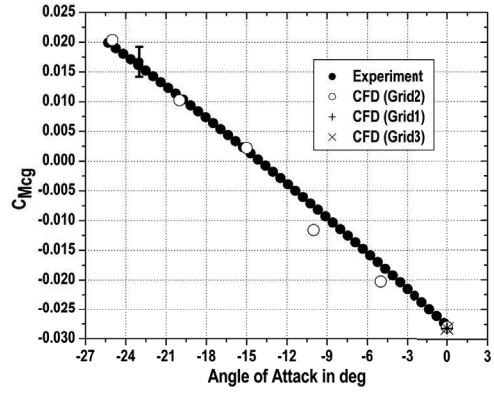


Figure 25. Comparison of C_{Mcg}.

data. In particular, the prediction of C_A with respect to the experimental values is well within the experimental uncertainty. However, it could be observed that as the angles-of-attack increases, the predicted values are consistently away from the experimental values. In general, as the angles-of-attack increases, the C_A decreases which is expected. On the other hand, excellent match is observed for predicted C_N and C_{Mcg} compared with the experimental results. As the angles-of-attack increases, the value of C_N increases which is the expected trend. In the case of C_{Mcg}, as the angles-of-attack increases, the capsule shows negative slope which indicates that the capsule is longitudinally stable. The trim angle of the vehicle is at $\alpha = -15^\circ$. The numerical simulation predicts C_{Mcg}, C_N and C_A within 8%, 4% and 3·5% respectively with respect to experimental values.

4.0 CONCLUSIONS

Numerical simulations are carried out to understand the flow features over a Crew Module at a freestream Mach number of 4 for different angles-of-attack ranging from 0 to –25º. Detailed flowfield analysis over the model in terms of contours of density gradient, numerical oil flow visualisation and near wake vortex structures are carried out. The prediction shows the typical shock patterns

https://doi.org/10.1017/S0001924000010794 Published online by Cambridge University Press

over the geometry and compared well with the experimental Schlieren images. The numerical oil flow shows the flow separation on the leeward side of the capsule starts at the shoulder region beyond –5º angles-of-attack and the separation moves upstream as the angles-of-attack increases. This is confirmed through the prediction of coefficient of skin friction on the leeward side. Another important parameter known as the location of sonic line is accurately predicted in the simulations. Also the near wake vortex structures and its characteristic behaviour due to angles-of-attack are captured in the present numerical simulations. The comparison of predicted C_P in two generators 0 and 90º shows excellent match with the experiment and the maximum value of C_P moves towards the shoulder of the windward side due to increasing angles-of-attack. The prediction of aerodynamic coefficients shows very good agreement with the experimental results. The numerical simulation predicts C_{Mcg}, C_N and C_A within 8%, 4% and 3·5%, respectively, with respect to experimental values.

ACKNOWLEDGEMENTS

The authors would like to thank V.R. Ganeasn, P. Balasubramanian and M. Prasath of the Experimental Aerodynamic Division, Vikram Sarabhai Space Centre, ISRO, Thiruvananthapuram for providing experimental data. The evaluation version of FLUENT software provided by Shri. Gopidas. R. Pai of ANSYS Software Private Ltd, Bangalore, India is greatly acknowledged.

REFERENCES

1. FUJIMOTO, K. and FUJII, K. Computational aerodynamic analysis of capsule configurations toward the development of reusable rockets, *J Spacecraft and Rockets*, 2006, **43**, (1), pp 77-83.
2. SCHNEIDER, S.P. Laminar-turbulent transition on reentry capsules and planetary probes, *J Spacecraft and Rockets*, 2006, **43**, (6), pp 115-1173.
3. VIVIANI, A. and PEZZELLA, G. Computational flowfield analysis over a blunt-body reentry vehicle, *J of Spacecraft and Rockets*, 2010, **47**, (2), pp 258-270.
4. SHARMA, M., SWANTEK, A.B., FLAHERTY, W., AUSTIN, J.M., DORAISWAMY, S. and CANDLER, G.V. Experimental and numerical investigation of hypervelocity carbon dioxide flow over blunt bodies, *J Thermophysics and Heat Transfer*, 2010, **24**, (4), pp 673-683.
5. METHA, R.C. Aerodynamic drag coefficient for various reentry configurations at high speed, AIAA-2006-3173.
6. JOHNSON, J.E, STARKEY, R.P. and LEWIS, M.J. Aerodynamic stability of reentry heat shield shapes for a crew exploration vehicle, *J Spacecraft and Rockets*, 2006, **43**, (4), pp 721-730.
7. MURPHY, K.J., BIBB, K.L., BRAUCKMANN, G.J., RHODE, M.N., OWENS, B., CHAN, D.T., WALKER, E.L., BELL, J.H. and WILSON, T.M. Orion Crew Module aerodynamic testing, AIAA-2011-3502.
8. BELL. J.H. Transonic/supersonic wind tunnel testing of the NASA Orion Command Module, AIAA-2007-1006.
9. CAMPBELL, C.C. and YECHOUT, T.R. Experimental evaluation of NASA Orion aerodynamic and stability characteristics, AIAA-2008-217.
10. ALLEGRE, J., RAFFIN, M., LENGRAND, J.C. and CHPOUN, A. Aerodynamic forces and moments for a re-entry module, *J Spacecraft and Rockets*, 1997, **34**, (2), pp 182-185.
11. MITVHELTREE, R.A., WILMOTH, R.G., CHEATWOOD, F.M., BRAUCKMANN, G.J. and GREENE, F.A. Aerodynamics of Stardust sample return capsule, AIAA-97-2304.
12. BIBB, K.L., WALKER, E.L., BRAUCKMANN, G.J. and ROBINSON, P.E. Development of the Orion crew module static aerodynamic database, Part I: Hypersonic, AIAA-2011-3506.
13. ZONG, J., OZAWA, T. and LEVIN, A. Comparison of high-altitude hypersonic wake flows of slender and blunt bodies, *AIAA J*, 2008, **48**, (1), pp 251-262.
14. BIBB, K.L., WALKER, E.L., BRAUCKMANN, G.J. and ROBINSON, P.E. Development of the Orion crew module static aerodynamic database, Part I: Hypersonic, AIAA-2011-3507.
15. SCHWING, A.M. and CANDLER, G.V. Validation of DES for capsule aerodynamics using 05-CA wind

https://doi.org/10.1017/S0001924000010794 Published online by Cambridge University Press

tunnel test data, AIAA-2013-0644.
16. LIEVER, P.A., HABCHI, S.D. BURNELL, S.I. and LINGARD, J.S. Computational fluid dynamics prediction of the Beagle 2 aerodynamic database, *J Spacecraft and Rockets*, 2003, **40**, (5), pp 632-638.
17. LIN, T.C., SPROUL, L.K., KIM, M., OLMOS. M. and FEIZ, H. Hypersonic reentry vehicle wake flow fields at angles of attack, AIAA-2006-582.
18. MACLEAN, M., MUNDY, E., WADHAMS, T., HOLDEN, M., BARNHARDT, M. and CANDLER, G. Experimental and numerical study of laminar and turbulent base flow on a spherical capsule, AIAA-2009-783.
19. KAWAI, S. and FUJII, K. Computational analysis of the characteristics of subsonic, transonic and supersonic base flows, AIAA-2005-5156.
20. VIVIANI, A., PEZZELLA, G. and CINQUEGRANA, D. Aerothermodynamics analysis of an Apollo-like reentry vehicle, AIAA-2006-8052.
21. GANESAN, V.R., BALASUBRAMANIAN, P. and PRASATH, M. Aero coefficients of Crew Module (CM) through wind tunnel tests in 1·2m wind tunnel, VSSC/ADD/TM-HSP/022/2010.
22. GANESAN, V.R. and BALASUBRAMANIAN, P. Crew module C_p distribution obtained through wind tunnel tests in 1·2m wind tunnel, VSSC/ADD/TM-HSP/032/2011.
23. LAMP, J.P. and OBERKAMPF, W.L. Review and development of base pressure and base heating correlation in supersonic flow, *J Spacecraft and Rockets*, 1995, **32**, (1), pp 8-23.

https://doi.org/10.1017/S0001924000010794 Published online by Cambridge University Press